Optimal Capacity Planning for Converter Stations in Sending-end MT-HVDC Systems Considering Uncertainties of PV Generation

Hao Lin, *Student Member*, *IEEE*, Liang Liang, *Senior Member*, *IEEE*, Haiqiong Yi, and Xiangjun Kong

***Abstract*—Sending-end multi-terminal high-voltage direct current (MT-HVDC) systems are well-suited for large-scale renewable energy collection and transmission. However, the capacity planning for converter stations (CSs), which is directly correlated with their ability to convert renewable energy, remains a critical issue. In this paper, an optimal capacity planning method for CSs is proposed to maximize the converted energy (CE). The proposed method considers the uncertainties of photovoltaic (PV) generation and derives analytical formulas for stochastic CEs. The equal incremental rate (EIR) principle is employed to calculate the optimal capacity planning scheme, and then a general guideline for the capacity planning in stochastic scenarios is presented. Case studies are conducted to validate the effectiveness of the proposed method and the proposed guideline. The results demonstrate that the proposed method converts more renewable energy than the deterministic method.**

***Index Terms*—Optimal capacity planning, converter station (CS), multi-terminal high-voltage direct current (MT-HVDC), equal incremental rate (EIR), renewable energy, uncertainty.**

I. Introduction

WITH the increasing global warming trend along with rapidly growing energy demand, the effective integration of renewable energy sources (RESs) has become a key challenge for nations worldwide. However, there exists a significant spatial gap between renewable-energy-rich regions and power load centers, particularly in China [1]. Multi-terminal high-voltage direct current (MT-HVDC) systems are well-suited to meet the demands for large-scale utilization of renewable energy and economical electricity transmission [2]. Nowadays, MT-HVDC projects have achieved remarkable success across the world. For example, in China, the Zhangbei [3] and Kunliulong [4] MT-HVDC projects are put into operation. In Europe, the NordLink MT-HVDC project connects the power grids of Germany and Norway via submarine cables, facilitating the exchange of renewable energy and the integration of the European energy market [5].

The MT-HVDC systems can be divided into three parts according to their roles and functions: the sending-end MT-HVDC system, the DC transmission corridor, and the receiving-end MT-HVDC system. Among these, the sending-end MT-HVDC system is responsible for collecting renewable power output and delivering it through the DC transmission corridor. In the sending-end MT-HVDC system, energy is collected by converter stations (CSs), and the sending-end MT-HVDC system delivers the converted energy (CE) to the load center for consumption. The inappropriate capacities of CSs can lead to negative effects, such as reducing CE and increasing project costs [6], [7]. Hence, it is worthwhile to explore the optimal capacity planning for MT-HVDC systems composed of CSs.

The planning of MT-HVDC system is a mathematical optimization problem, which can generally be solved using mixed-integer nonlinear programming (MINLP) or other models. Previous studies mainly focus on the interconnection planning of MT-HVDC systems. In [8], a topology planning method for voltage source converter based MT-HVDC (VSC-MT-HVDC) from a reliability perspective is introduced. A bi-level and multi-objective nonlinear model is developed to tackle the optimal allocation problem of the power flow controller. Reference [9] examines the dynamic construction of offshore infrastructures and proposes an nonlinear model to optimize the MT-HVDC system. The model proposed in [9] maximizes the revenues of the power grid throughout economic lifetime. A mixed-integer nonlinear optimization model is proposed in [10] to plan the grid topology of a submarine MT-HVDC system. The computational results demonstrate the effectiveness of the model proposed in [10]. Regarding the capacity planning method, [11] proposes a two-layer multi-objective optimization model to determine the optimal capacity planning scheme of CSs in a DC distribution system. Reference [12] investigates an optimal plan-

Manuscript received: August 26, 2024; revised: January 15, 2025; accepted: May 5, 2025. Date of CrossCheck: May 5, 2025. Date of online publication: August 1, 2025.

This work was supported by National Natural Science Foundation of China (No. 52077045) and Shenzhen-Hong Kong-Macau Science and Technology Program (category C) (No. SGDX20220530111403026).

H. Lin and L. Liang (corresponding author) are with the School of Mechanical Engineering and Automation, Harbin Institute of Technology, Shenzhen, China (e-mail: 25b353017@stu.hit.edu.cn; liangl@hit.edu.cn).

H. Yi is with the Department of Transmission Planning, State Grid Economic and Technological Research Institute Co., Ltd., Beijing, China (e-mail: yihaiqiong@chinasperi.sgcc.com.cn).

X. Kong is with the Electric Power Dispatching and Communication Center, State Grid Shanghai Municipal Electric Power Company, Shanghai, China (e-mail: kongxiangjun@sh.sgcc.com.cn).

DOI: 10.35833/MPCE.2024.000949

ning method for a bundled wind-thermal MT-HVDC system. A nonlinear model is presented to address the coordinated planning of the optimal rated voltage, capacities of CSs, and transmission capacity of the MT-HVDC system. The results of case studies demonstrate that the model proposed in [12] effectively minimizes the unit generation cost.

The aforementioned studies have addressed the planning problem for MT-HVDC systems by mathematical modeling, whereas the optimized results are all calculated in deterministic scenarios. However, due to the complex weather conditions in the natural world, the output power of RESs is inherently volatile and unpredictable [13]. To address these uncertainties, stochastic optimization methods are employed in previous research, which can be categorized into two main methods: the scenario-based numerical method and the analytical method [14]. Reference [15] presents an optimal dispatch model, which is established to mitigate the negative impact caused by wind fluctuation. A two-stage stochastic planning model is developed and the uncertainties are addressed through analytical method. In [16], a scenario-based probabilistic sizing method is applied in the MT-HVDC system to reduce the operation cost. This method uses probability distribution functions (PDFs) to represent the uncertainties of RESs and the validity of the method is verified through numerical calculation. Robust optimization methods are also employed to handle the uncertainties. Reference [17] applies the robust optimization method to tackle the transmission expansion planning (TEP) problems of the MT-HVDC system. The unpredictability and intermittency of RESs are incorporated into the optimization, and the worst scenario is investigated. Reference [18] proposes a robust framework for security-constrained unit commitment (SCUC) dispatch, considering the regulation of MT-HVDC system. Extreme uncertainties of RESs are taken into account and an MINLP model is presented for security operation. Comparing stochastic optimization method and robust optimization method, stochastic optimization method depends on PDFs for model construction and scenario generation, whereas robust optimization method utilizes bounded intervals to represent the uncertainties. Given that the stochastic photovoltaic (PV) generation can be described using PDFs, the scenario-based numerical method is adopted in this study.

Our previous work [19] investigates the optimal capacity planning method for a sending-end MT-HVDC system with a deterministic background. A multi-constrained quadratic programming model is proposed in [19] to derive the planning scheme. However, this model is grounded in deterministic scenario and ignoring the stochastic PV generation. Existing studies focus on the stable and economic operation of MT-HVDC systems in stochastic scenarios, but none of them targets the maximization of CE for CSs. Therefore, in this study, the uncertainties of PV generation are considered, and an optimal capacity planning method is proposed to determine the optimal capacity planning scheme for CSs in the sending-end MT-HVDC system.

The contributions can be summarized as follows.

1) Analytical formulas for stochastic CEs are derived based on the Beta-distributed PV generation.

2) Considering the Lagrange multiplier method based on Karush-Kuhn-Tucker (KKT) conditions, the equal incremental rate (EIR) principle is applied to determine the optimal capacity planning scheme for CSs.

3) A guideline for capacity planning is proposed, considering uncertainties of PV generation.

The remainder of this paper is organized as follows. Section II presents the deterministic method for capacities of CSs. In Section III, the capacity planning in stochastic scenarios is presented. Subsequently, the guideline for optimal capacity planning in stochastic scenarios is presented in Section IV. Section V examines case studies to validate the proposed method and the guideline. Finally, Section VI concludes this paper.

II. Deterministic Method for Capacities of CSs

A. Model of Sending-end MT-HVDC System

The typical structure of four-terminal sending-end MT-HVDC system investigated in this paper is shown in Fig. 1, where several CSs are interconnected to form a ring network.

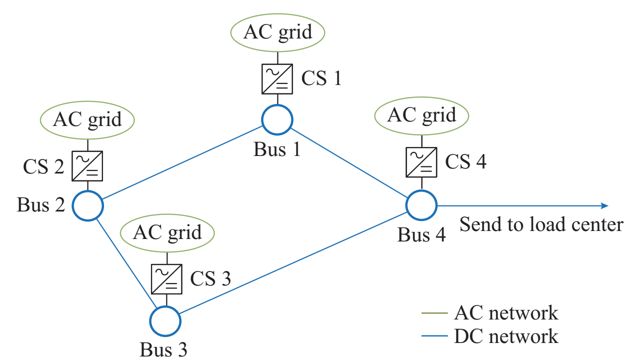

Fig. 1. Typical structure of four-terminal sending-end MT-HVDC system.

The local AC grid aggregates the energy generated by PV plants and transmits it to the CS for energy conversion, as illustrated in Fig. 2(a). The input power of CS is defined as the AC power from local AC network, whereas the output power of the CS is defined as the DC power injected into the sending-end MT-HVDC system.

Considering the capacity constraint of CS, the relationship between input AC power and output DC power is shown as (1). The higher the power flowing through the system, the greater the relative loss of CS.

$$P_{C,t}^{\mathrm{CS,out}} = \begin{cases} \tilde{\eta} P_t^{\mathrm{CS,in}} & \tilde{\eta} P_t^{\mathrm{CS,in}} \le C \\ C & \text{otherwise} \end{cases} \tag{1}$$

where C is the capacity constraint of CS, which refers to the maximum converted power; $\tilde{\eta}$ is the efficiency of CS, taking 0.98-0.99 as the typical values [6]; $P_t^{\mathrm{CS,in}}$ is the input AC power of CS at time t; and $P_{C,t}^{\mathrm{CS,out}}$ is the output DC power under capacity constraint C at time t.

In this paper, CE denotes the DC energy injected into the sending-end MT-HVDC system from CSs. As shown in Fig. 2(b), CE refers to the integral of the output DC power curve with respect to time, i.e., the area of the shaded part. The integral of the continuous curve can be transformed into the sum of discrete quantities by using the infinitesimal element method. Thus, the CE of a CS is expressed as:

$$E_{CE,dtm}(C)=\int_{t_1}^{t_n} P_{C,t}^{\mathrm{CS,out}}\mathrm{d}t=\sum_{t=1}^{n} P_{C,t}^{\mathrm{CS,out}}\Delta t=\sum_{t=1}^{8760} P_{C,t}^{\mathrm{CS,out}} \tag{2}$$

where $E_{CE,dtm}(C)$ is the CE during time t_1 and t_n under capacity constraint C; Δt is the time interval; and n is the maximum number of time intervals. In (2), we set Δt as 1 hour and n as 8760. Therefore, (2) denotes the one-year CE under capacity constraint C.

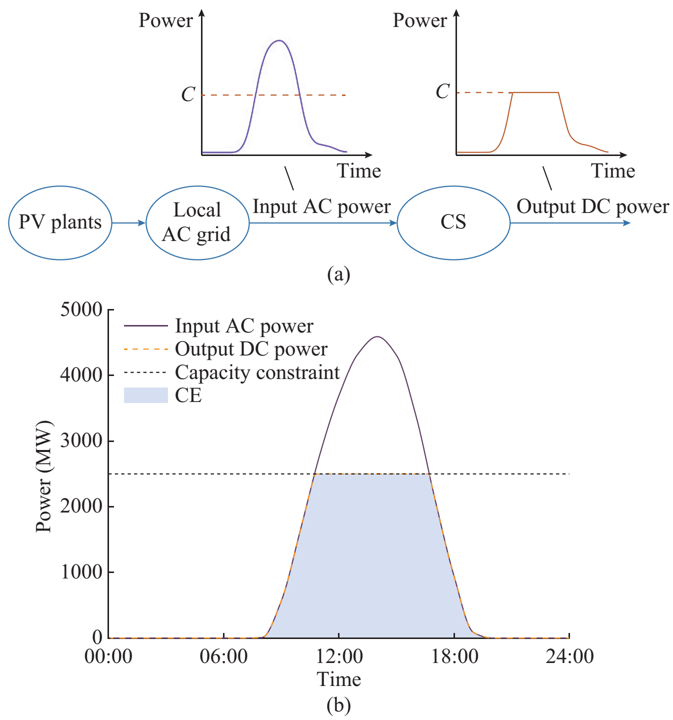

Fig. 2. Energy conversion process for CS and definition of CE. (a) Input AC power and output DC power of CS. (b) Capacity constraint and CE of CS.

For a deterministic input AC power data, a different $E_{CE,dtm}(C)$ can be calculated with a different C according to (1) and (2). Based on this one-to-one corresponding relationship between $E_{CE,dtm}(C)$ and C, the converted energy-capacity (CE-C) curve is plotted. The flow chart of CE-C curve plotting is shown in Fig. 3 and an example of the CE-C curve is shown in Fig. 4. In Fig. 4, the x-axis indicates different calculation scenarios with different capacity constraints and y-axis indicates the corresponding CEs. When the gaps between discrete points are small enough, the appearance of the CE-C curve tends to be smooth.

B. Optimal Capacity Planning Based on EIR Principle

The sending-end MT-HVDC system consists of several CSs, each of which corresponds to a different CE-C curve. For the highest profit, one must maximize the total CEs of all CSs through an optimal capacity planning scheme constrained by the planned capacity threshold. The mathematical model is illustrated as follows.

The objective function is to maximize the sum of each CE from all CSs, which is given as:

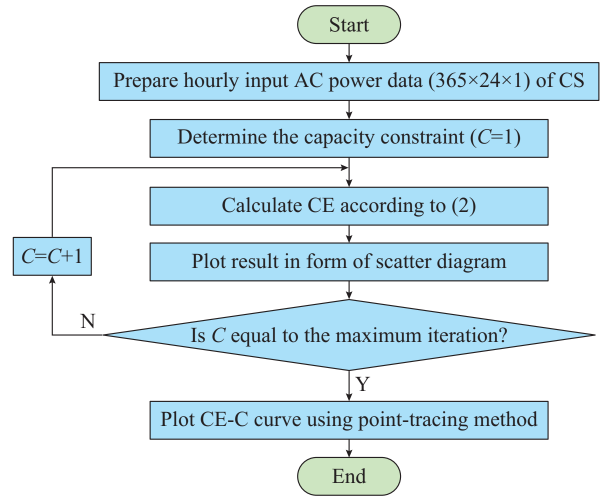

Fig. 3. Flow chart of CE-C curve plotting.

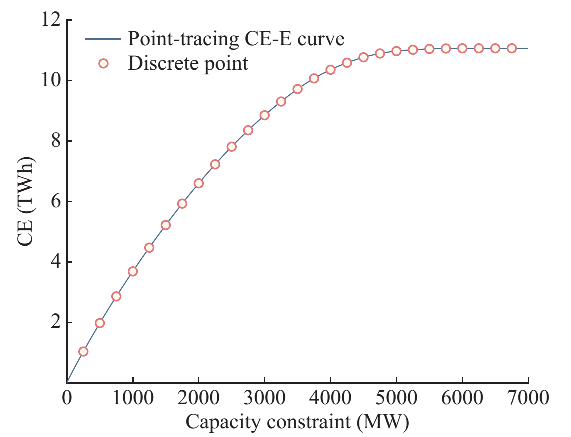

Fig. 4. Example of CE-C curve.

$$\max E=\sum_{i=1}^{m} E_{CE,i}(C_i) \tag{3}$$

s.t.

$$\sum_{i=1}^{m} C_i - C_{total}=0 \tag{4}$$

where E is the objective function; $E_{CE,i}(C_i)$ is the CE of CS i, whose capacity is C_i; C_{total} is the planned capacity threshold of a sending-end MT-HVDC system, which is kept unchanged; and m is the number of CSs.

Lagrange multiplier method based on the KKT conditions is introduced. The incremental rate (IR) of the CE-C curve is defined as (5). According to differential-element method, the straight-line slope of two adjacent discrete points on the CE-C curve is taken as the IR.

$$IR(C_i)=\frac{E_{CE,i}(C_{i+1})-E_{CE,i}(C_i)}{C_{i+1}-C_i}=\frac{\mathrm{d}E_{CE,i}(C_i)}{\mathrm{d}C_i} \tag{5}$$

where $IR(C_i)$ is the IR of the CE-C curve at capacity C_i.

Because of the single-peak shape of the PV output curve, as the capacity increases, the increase in shadow of Fig. 2(a) (i.e., the IR of CE-C curve) gradually decreases.

Given that the objective function increases monotonically, the Lagrange multiplier λ is introduced for the constraint (4), and the objective function in (3) is extended to Φ_M, which is given as:

$$\Phi_M = \max\left(\sum_{i=1}^{m} E_{CE,i}(C_i) - \lambda\left(\sum_{i=1}^{m} C_i - C_{total}\right)\right) \tag{6}$$

Thus, solving the extremum problem of the objective function (3) under constraint (4) is transformed into the non-extremum problem of Φ_M, where the variables to be solved are C_i and λ. All the partial derivatives of Φ_M for $E_{CE,i}(C_i)$ are found, assuming that they are equal to zero. The conditions for the existence of extreme values of Φ_M are shown in (7), namely the KKT conditions.

$$\begin{cases} \dfrac{\partial \Phi_M}{\partial C_i} = \dfrac{E_{CE,i}(C_i)}{\partial C_i} - \lambda = 0 \quad i = 1, 2, \ldots, m \\ \dfrac{\partial \Phi_M}{\partial \lambda} = 0 \end{cases} \tag{7}$$

It is assumed that:

$$\frac{\partial E_{CE,i}(C_i)}{\partial C_i} = \frac{\mathrm{d}E_{CE,i}(C_i)}{\mathrm{d}C_i} = \lambda_i \tag{8}$$

where λ_i is the IR of $E_{CE,i}(C_i)$.

By solving (7) and (8), the condition for the existence of extreme values is equivalent to (9).

$$\lambda_1 = \lambda_2 = \ldots = \lambda_m = \lambda \tag{9}$$

Formula (9) indicates that the objective function, i.e., the sum of CEs, reaches its extreme value when IRs of all $E_{CE,i}(C_i)$ are equal. Given the convex shape and monotonically increasing feature of the CE-C curve, its extreme value is equivalent to the global maximum value. This approach of identifying the extreme points using IR is known as the EIR principle [20]. The schematic diagram of EIR principle applied in this study is illustrated in Fig. 5, where θ denotes the IRs of points C_1, C_2, and C_3. In Fig. 5, the equal IRs of three curves at points C_1, C_2, and C_3 indicate that the planning scheme $[C_1, C_2, C_3]$ is optimized.

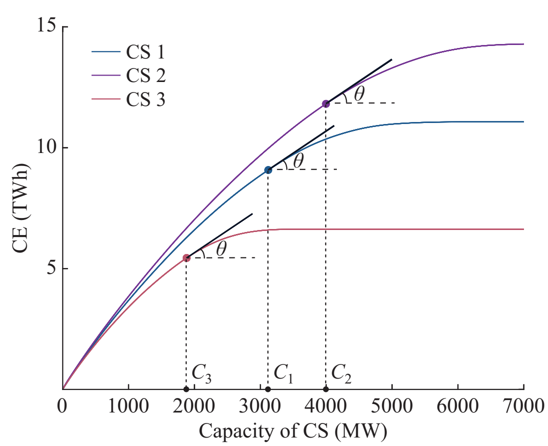

Fig. 5. Schematic diagram of EIR principle.

III. Capacity Planning in Stochastic Scenarios

A. Probabilistic PV Generation

Owing to unpredictable weather conditions, such as clouds passing over the PV plants and rainy days, the PV output at a specific time frame in each day tends to be variable and uncertain. In this study, a set of hourly PV output data in northwest China [21] is used, as shown in Fig. 6.

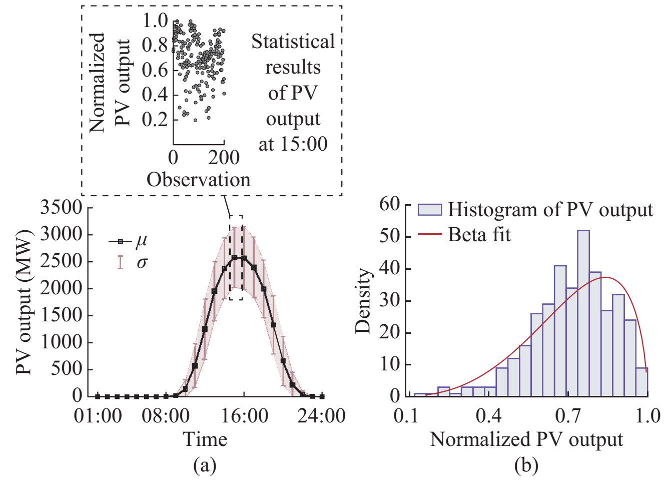

Fig. 6. Probabilistic PV generation. (a) Daily PV output. (b) Histogram of PV output at 15:00.

Figure 6(a) shows the daily PV output curve with mean μ and standard deviation σ. Do the distribution test for the historical data at 15:00. The results are shown in Fig. 6(b). The histogram of PV output at 15:00 shows that the PV output at 15:00 can be modelled by a function following Beta distribution, which is widely used for probabilistic solar irradiance and PV generation in [22]-[24]. In this paper, the hourly PV output across different days is assumed to follow a Beta distribution, whose PDF is shown as:

$$f_{\mathrm{PDF}}(s_t) = \frac{\Gamma(\alpha_t + \beta_t)}{\Gamma(\alpha_t)\Gamma(\beta_t)}\left(\frac{s_t}{s_{t,\max}}\right)^{\alpha_t - 1}\left(1 - \frac{s_t}{s_{t,\max}}\right)^{\beta_t - 1} \tag{10}$$

$$\alpha_t = \mu_t\left[\frac{\mu_t(1-\mu_t)}{\sigma_t^2} - 1\right] \tag{11}$$

$$\beta_t = (1-\mu_t)\left[\frac{\mu_t(1-\mu_t)}{\sigma_t^2} - 1\right] \tag{12}$$

where s_t is the Beta-distributed random variable for PV outputs at time t; $s_{t,\max}$ is the maximum value of s_t; $f_{\mathrm{PDF}}(s_t)$ is the PDF of the random variable s_t; $\Gamma(\cdot)$ is the Gamma function; α_t and β_t are the shape parameters of the Beta distribution, and their values are determined by historical data; and μ_t and σ_t are the mean value and standard deviation of the PV output at time t, respectively.

B. Stochastic CEs Considering Uncertainties

Based on the assumption of probabilistic PV generation, the input AC power of CS at the same time each day is regarded as a Beta-distributed random variable, as shown in (13).

$$\tilde{\eta} P_{t_h,t_d}^{\mathrm{CS,in}} \sim Beta(\alpha_{t_h}, \beta_{t_h}) \tag{13}$$

where $t_h = 1, 2, \ldots, 24$ denotes the hour; $t_d = 1, 2, \ldots, 365$ denotes the day; and $P_{t_h,t_d}^{\mathrm{CS,in}}$ is the stochastic input AC power of

CS at hour t_h in day t_d, which obeys the Beta distribution with parameters α_{t_h} and β_{t_h} $Beta(\alpha_{t_h},\beta_{t_h})$.

α_{t_h} and β_{t_h} in (13) are obtained through statistical analysis of the historical PV output data. It is noted that the probability distributions of $\tilde{\eta}P^{\text{CS, in}}_{t_h,t_d}$ and $P^{\text{CS, in}}_{t_h,t_d}$ are regarded as the same because of the high efficiency of the CS.

Considering the capacity constraint, the probability distribution of output power of CS $P^{\text{CS, out}}_{C,t_h,t_d}$ is shown in Fig. 7. According to (1), the analytical formulas for PDF of $P^{\text{CS, out}}_{C,t_h,t_d}$ are derived as follows.

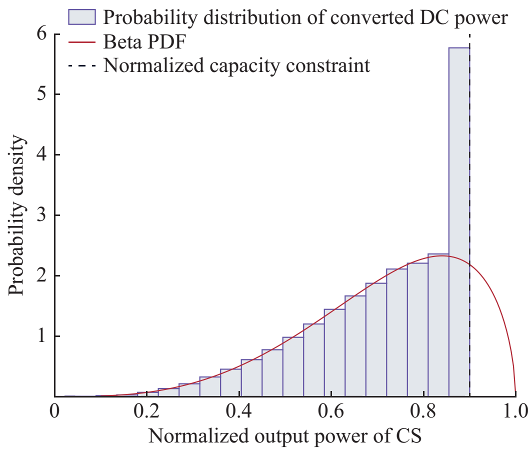

Fig. 7. Probability distribution of $P^{\text{CS, out}}_{C,t_h,t_d}$.

When $P^{\text{CS, in}}_{t_h,t_d}$ is less than C, the PDF $f_{\text{PDF}}(P^{\text{CS, out}}_{C,t_h,t_d})$ is denoted as:

$$f_{\text{PDF}}(P^{\text{CS, out}}_{C,t_h,t_d})=\frac{\Gamma(\alpha_{t_h}+\beta_{t_h})}{\Gamma(\alpha_{t_h})\Gamma(\beta_{t_h})}(\tilde{\eta}P^{\text{CS, in}}_{t_h,t_d})^{\alpha_t-1}(1-\tilde{\eta}P^{\text{CS, in}}_{t_h,t_d})^{\beta_t-1} \tag{14}$$

s.t.

$$\begin{cases}\tilde{\eta}P^{\text{CS, in}}_{t_h,t_d}\leq C\\ P^{\text{CS, out}}_{C,t_h,t_d}=\tilde{\eta}P^{\text{CS, in}}_{t_h,t_d}\end{cases} \tag{15}$$

When $P^{\text{CS, in}}_{t_h,t_d}$ is greater than C, the PDF $f_{\text{PDF}}(P^{\text{CS, out}}_{C,t_h,t_d})$ is denoted as:

$$f_{\text{PDF}}(P^{\text{CS, out}}_{C,t_h,t_d})=\int_C^1\frac{\Gamma(\alpha_{t_h}+\beta_{t_h})}{\Gamma(\alpha_{t_h})\Gamma(\beta_{t_h})}(\tilde{\eta}P^{\text{CS, in}}_{t_h,t_d})^{\alpha_t-1}(1-\tilde{\eta}P^{\text{CS, in}}_{t_h,t_d})^{\beta_t-1}\mathrm{d}\tilde{\eta}P^{\text{CS, in}}_{t_h,t_d} \tag{16}$$

s.t.

$$\begin{cases}\tilde{\eta}P^{\text{CS, in}}_{t_h,t_d}>C\\ P^{\text{CS, out}}_{C,t_h,t_d}=C\end{cases} \tag{17}$$

In (14)-(17), $P^{\text{CS, in}}_{t_h,t_d}$ is normalized within the interval of $[0,1]$. In addition, C is also normalized, with its value determined relative to that of $P^{\text{CS, in}}_{t_h,t_d}$. Formulas (14)-(17) analytically express the distribution shape of Fig. 7. The expectation and variance of $P^{\text{CS, out}}_{C,t_h,t_d}$ are shown in (18) and (19), respectively. The detailed derivation process and the numerical evidences are provided in Supplementary Material A.

$$\mathbb{E}[P^{\text{CS, out}}_{C,t_h,t_d}]=\frac{\alpha_{t_h}}{\alpha_{t_h}+\beta_{t_h}}F_{\text{CDF}}(C;\alpha_{t_h}+1,\beta_{t_h})+C(1-F_{\text{CDF}}(C;\alpha_{t_h},\beta_{t_h})) \tag{18}$$

$$\mathbb{D}[P^{\text{CS, out}}_{C,t_h,t_d}]=\frac{\alpha_{t_h}(\alpha_{t_h}+1)}{(\alpha_{t_h}+\beta_{t_h})(\alpha_{t_h}+\beta_{t_h}+1)}F_{\text{CDF}}(C;\alpha_{t_h}+2,\beta_{t_h})+C^2\cdot(1-F_{\text{CDF}}(C;\alpha_{t_h},\beta_{t_h}))]-(\mathbb{E}[P^{\text{CS, out}}_{C,t_h,t_d}])^2 \tag{19}$$

$$F_{\text{CDF}}(x;\alpha,\beta)=\frac{\Gamma(\alpha+\beta)}{\Gamma(\alpha)\Gamma(\beta)}\int_0^x t^{\alpha-1}(1-t)^{\beta-1}\mathrm{d}t \tag{20}$$

where $\mathbb{E}[P^{\text{CS, out}}_{C,t_h,t_d}]$ and $\mathbb{D}[P^{\text{CS, out}}_{C,t_h,t_d}]$ are the expectation and variance of $P^{\text{CS, out}}_{C,t_h,t_d}$, respectively; and $F_{\text{CDF}}(x;\alpha,\beta)$ is the Beta cumulative distribution function (CDF) with distribution parameters α and β; and $F_{\text{CDF}}(C;\alpha,\beta)$ is the CDF value where x equals to C.

In (2), the CE of a CS during one year is expressed by the sum of $P^{\text{CS, out}}_{C,t_h,t_d}$, which is classified according to hours and days. The classification for $P^{\text{CS, out}}_{C,t_h,t_d}$ is shown in Fig. 8, where CLT is short for central limit theorem.

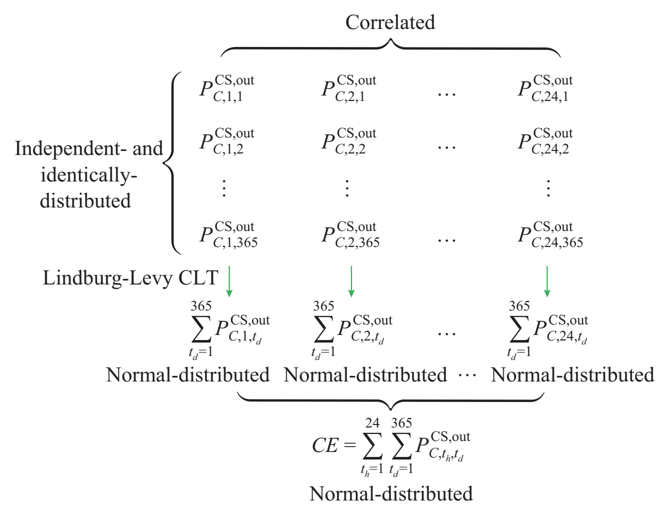

Fig. 8. Classification for $P^{\text{CS, out}}_{C,t_h,t_d}$.

Due to the highly correlated weather conditions (including solar irradiance) at adjacent moments [25], $P^{\text{CS, out}}_{C,t_h,t_d}$ (t_d remains unchanged) at adjacent hours tends to be dependent. Hence, the Pearson correlation coefficient $\rho_{X,Y}$ is employed to indicate this relationship, as shown in (21).

$$\rho_{X,Y}=\frac{Cov(X,Y)}{\sqrt{\mathbb{D}[X]\mathbb{D}[Y]}}=\frac{\mathbb{E}[XY]-\mathbb{E}[X]\mathbb{E}[Y]}{\sqrt{\mathbb{D}[X]\mathbb{D}[Y]}} \tag{21}$$

where X and Y are two random variables; $\mathbb{E}[X]$ and $\mathbb{D}[X]$ are the expectation and variance of X, respectively; and $Cov(X,Y)$ is the covariance between X and Y.

The value interval of $\rho_{X,Y}$ is $[-1,1]$, where -1 indicates absolutely negatively correlated, 1 indicates absolutely positively correlated, and 0 indicates no correlation.

To quantify the temporal correlation of PV output, numerical calculation is conducted. The process is as follows.

1) Prepare hourly PV output data ($365\times24\times1$) and classify these data into 24 sets according to hours.

2) For each set of data, apply fast Fourier transform

(FFT) method [26] to filter the seasonal periodic component and classify these data into 24 sets according to hours.

3) Calculate the daily fluctuations (actual daily values minus the mean of a year) for each set of data.

4) Select the daytime sets and calculate the Pearson correlation coefficients. Choose the data at 15:00 and do the autocorrelation test. The results of correlation test are shown in Fig. 9.

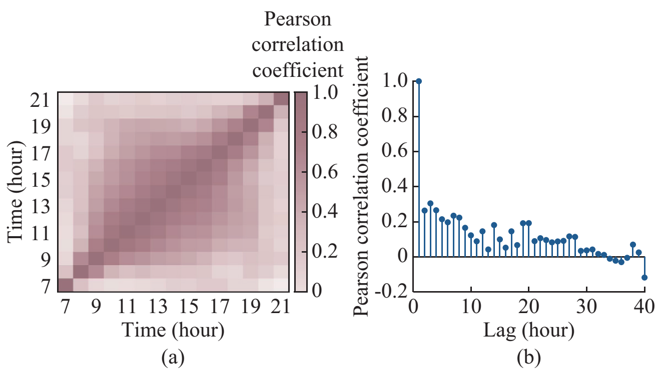

Fig. 9. Results of correlation test. (a) Temporal correlation of PV fluctuation. (b) Autocorrelation test of daily PV fluctuation at 15:00.

Figure 9(a) is the heatmap of Pearson correlation coefficient matrix, representing the temporal correlation of the PV fluctuation at different hours, i. e., the temporal correlations between $P_{7,t_d}^{\mathrm{CS,in}}, P_{8,t_d}^{\mathrm{CS,in}}, ..., P_{21,t_d}^{\mathrm{CS,in}}$ (t_d remains unchanged). According to the results, the adjacent hours have the highest correlation level (with Pearson correlation coefficient exceeds 0.6) compared with other moments. Such results align with the theoretical findings in [27]. Figure 9(b) depicts the results of autocorrelation test of a daily PV fluctuation at 15: 00, i. e., the correlation between $P_{15,1}^{\mathrm{CS,in}}, P_{15,2}^{\mathrm{CS,in}}, ..., P_{15,365}^{\mathrm{CS,in}}$. The results indicate a relatively weak correlation (with Pearson correlation coefficient below 0.3) between the PV output at the same moment across different days. Regarding this, the PV generation at the same moment in different days are assumed to be independent, whereas the correlation between adjacent hours is considered.

In other words, $P_{t_h,1}^{\mathrm{CS,in}}, P_{t_h,2}^{\mathrm{CS,in}}, ..., P_{t_h,365}^{\mathrm{CS,in}}$ (t_h remains unchanged) are assumed to be independent, with the same Beta-distributed parameters in (13). After being constrained by the capacity of CS, $P_{C,t_h,1}^{\mathrm{CS,out}}, P_{C,t_h,2}^{\mathrm{CS,out}}, ..., P_{C,t_h,365}^{\mathrm{CS,out}}$ are also regarded as independent- and identically-distributed random variables, whose distribution shape is shown in Fig. 7. According to the Lindburg-Levy CLT illustrated in Fig. 8, the sum of $P_{C,t_h,t_d}^{\mathrm{CS,out}}$ (t_h remains unchanged) can be regarded as normal-distributed random variables, with analytical formulas in (22).

$$\sum_{t_d=1}^{365} P_{C,t_h,t_d}^{\mathrm{CS,out}} \sim N(\mu_{t_h}, \sigma_{t_h}^2) \tag{22a}$$

$$\mu_{t_h} = \sum_{t_d=1}^{365} \mathbb{E}[P_{C,t_h,t_d}^{\mathrm{CS,out}}] \tag{22b}$$

$$\sigma_{t_h}^2 = \sum_{t_d=1}^{365} \mathbb{D}[P_{C,t_h,t_d}^{\mathrm{CS,out}}] \tag{22c}$$

where $N(\mu, \sigma)$ denotes to the normal distribution.

As depicted in Fig. 8, CE is denoted by the sum of 24 correlated normal-distributed random variables. Hence, the analytical formulas for stochastic CEs $E_{CE,sto}(C)$ are shown in (23), with analytical expectation and variance.

$$E_{CE,sto}(C) = \sum_{t_h=1}^{24} \sum_{t_d=1}^{365} P_{C,t_h,t_d}^{\mathrm{CS,out}} \sim N(\mu, \sigma^2) \tag{23a}$$

$$\mu = \sum_{t_h=1}^{24} \mu_{t_h} \tag{23b}$$

$$\sigma^2 = \sum_{t_h=1}^{24} \sigma_{t_h}^2 + \sum_{1 \le p < q \le 24} 2Cov\left(\sum_{t_d=1}^{365} P_{C,p,t_d}^{\mathrm{CS,out}}, \sum_{t_d=1}^{365} P_{C,q,t_d}^{\mathrm{CS,out}} \right) \tag{23c}$$

where $E_{CE,sto}(C)$ is the expectation of stochastic CEs.

The stochastic CEs (i.e., the CE results considering PV uncertainties) are assumed to follow normal distribution. The reason is demonstrated as follows. For Fig. 9(a), the computational results show that the Pearson correlation matrix is a positive definite correlation matrix. This means, the PV outputs at different hours, i. e., $P_{p,t_d}^{\mathrm{CS,in}}$ and $P_{q,t_d}^{\mathrm{CS,in}}$ ($p \ne q$), are not absolutely correlated ($\rho \ne 1$ or $\rho \ne -1$). In this study, weather conditions are regarded as the primary factor driving temporal correlations. Consequently, it is approximated that only linear correlations exist between $P_{p,t_d}^{\mathrm{CS,in}}$ and $P_{q,t_d}^{\mathrm{CS,in}}$. Under the aforementioned two conditions (i.e., the positive definite correlation matrix and the linear correlation), the joint distribution of these 24 normal variables is modeled as a normal distribution. Based on the properties of the joint normal distribution, any linear combination (including the sum) of these variables follows a normal distribution. Therefore, the stochastic CEs can be represented by a new normal-distributed random variable, as shown in (23a). The normal-distributed stochastic CEs are confirmed in Supplemental Material B, which validates the aforementioned explanation.

Actually, the assumption for the derivation of CLT can be further generalized. As long as the uncertainties of the PV output can be described using analytical formulas, such as Gaussian and Weibull, the same final conclusion can be derived. By modifying (18) and (19) to align with the assumption, the normal-distributed variables of the stochastic CE can be obtained through (22) and (23). Moreover, even if the uncertainties cannot be described by a single PDF, the normal-distributed results can still be derived through the expansion form of the CLT [28], which posits that the distribution shapes of different stochastic formulas are sufficiently similar. These analyses demonstrate that the theoretical findings in this work have the potential for broader applicability in different scenarios.

C. EIR Principle Based on Stochastic CE-C Curves

In the deterministic scenario, the CE-C curve is calculated based on the historical data. When considering uncertainties, the PV output data vary in different scenarios, leading to the corresponding changes in the optimal planning scheme. Nevertheless, it is possible to confirm a planning scheme according to the stochastic assumption, maximizing the expected profit in stochastic scenarios.

Based on the analysis in Section III-B, the stochastic CEs are modeled as normal-distributed variables. Using this probabilistic framework, the stochastic CEs under different capacities are obtained according to (18) and (23). The stochastic CE-C curve, which represents the expected value with confidence interval, is derived from the computational results of stochastic CEs for different capacities. Since the IR of the stochastic CE-C curve decreases monotonically (shown in Supplemental Material A), the methodology of EIR is still valid. Consequently, the optimal capacity planning method proposed in this paper can be summarized as follows.

1) First, identify the CSs in the sending-end MT-HVDC system and obtain the historical PV output data for each CS.

2) Then, calculate the stochastic CE-C curves for different CSs according to their respective historical data and stochastic assumptions.

3) Finally, EIR principle is employed to calculate the optimal capacity planning scheme based on the stochastic CE-C curves.

Figure 10 depicts the deterministic CE-C curve and stochastic CE-C curve. The deterministic CE-C curve is plotted using the deterministic method demonstrated in Section II, while stochastic CE-C curve is obtained through the proposed method in Section III. These two curves are computed based on the same historical data, which explains why the results of CEs calculated by the two methods tend to be equal when the capacity is sufficiently large.

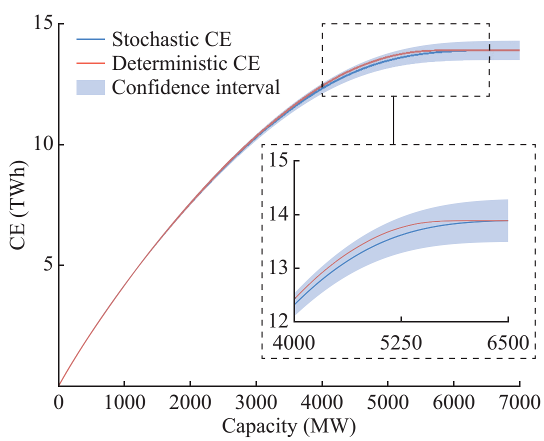

Fig. 10. Deterministic CE-C curve and stochastic CE-C curve.

IV. Guideline for Optimal Capacity Planning in Stochastic Scenarios

A. Quantitative Relationship Between Stochastic and Deterministic CE-C Curves

According to Fig. 7, the capacity constraint limits the probability of output DC power. Consequently, the expected value of CE is lower than that in the deterministic scenario, where such constraints are absent. This explains why the stochastic CE-C curve is lower than the deterministic CE-C curve in Fig. 10. When the capacity of CS is sufficiently large or small, these two CE-C curves converge to the same one.

Since the capacity planning scheme is computed based on the EIR principle, particular attention is given to the relationship of IRs of the above-mentioned two CE-C curves. To quantify the relationship between the two CE-C curves, the analytical formula for the IR of stochastic CE-C curve is expressed as:

$$IR_{sto}(C)=\frac{\partial E_{CE,sto}(C)}{\partial C}=\sum_{t_h=1}^{24}\sum_{t_d=1}^{365}\frac{\partial \mathbb{E}[P_{C,t_h,t_d}^{\text{CS,out}}]}{\partial C} \tag{24}$$

where $IR_{sto}(C)$ is the IR of stochastic CE-C curve under capacity constraint C.

According to (18), the partial differential of $P_{C,t_h,t_d}^{\text{CS,out}}$ is expressed as:

$$\frac{\partial \mathbb{E}[P_{C,t_h,t_d}^{\text{CS,out}}]}{\partial C}=\frac{\alpha_{t_h}}{\alpha_{t_h}+\beta_{t_h}}f_{\text{PDF}}(C;\alpha_{t_h}+1,\beta_{t_h})+1-F_{\text{CDF}}(C;\alpha_{t_h},\beta_{t_h})-Cf_{\text{PDF}}(C;\alpha_{t_h},\beta_{t_h}) \tag{25}$$

For deterministic CE-C curve, the IR $IR_{dtm}(C)$ is expressed as:

$$IR_{dtm}(C)=E_{CE,dtm}(C+1)-E_{CE,dtm}(C)=\sum_{t=1}^{8760}(P_{C+1,t}^{\text{CS,out}}-P_{C,t}^{\text{CS,out}}) \tag{26}$$

where $IR_{dtm}(C)$ is the IR of deterministic CE-C curve.

In addition, $P_{C,t}^{\text{CS,out}}$ is represented in forms of the piecewise function, as shown in (1). Hence, the IR values of $P_{C,t}^{\text{CS,out}}$ also need to be discussed categorically. When the input AC power is lower than C, the output DC power increases linearly with the input AC power. When input AC power exceeds C, the output DC power remains the same as the input AC power. This relationship is described as:

$$P_{C+1,t}^{\text{CS,out}}-P_{C,t}^{\text{CS,out}}=\begin{cases}\tilde{\eta} & \tilde{\eta}P_t^{\text{CS,in}}\leq C\\ 0 & \text{otherwise}\end{cases} \tag{27}$$

Given that the loss of CS is small enough, $\tilde{\eta}$ is approximated to 1 in the following context.

By performing the subtraction between (24) and (26), the incremental rate difference (IRD) $IRD(C)$ is calculated as:

$$IRD(C)=IR_{sto}(C)-IR_{dtm}(C) \tag{28}$$

According to (28), the IRD of CE-C curves is computed. By changing the value of C to cover all points in the CE-C curve, the corresponding relationship between IRD and C is obtained. The numerical evidences in Supplementary Material C validate (24)-(28).

B. Analysis for IRD Curve and Guideline for Capacity Planning

Based on the proposed analytical formulas, two IRD samples are plotted in Fig. 11(a). The fluctuation amplitude of PV resource is considered, according to Beta-distributed parameters in (10)-(12). By changing the parameters of the Beta distribution, scenarios under different PV fluctuations can be represented. In high PV fluctuation scenario, the variance is larger, whereas in low PV fluctuation scenario, it is reversed. In both the high and low PV fluctuation scenarios, the expectations of the Beta distributions remain the same.

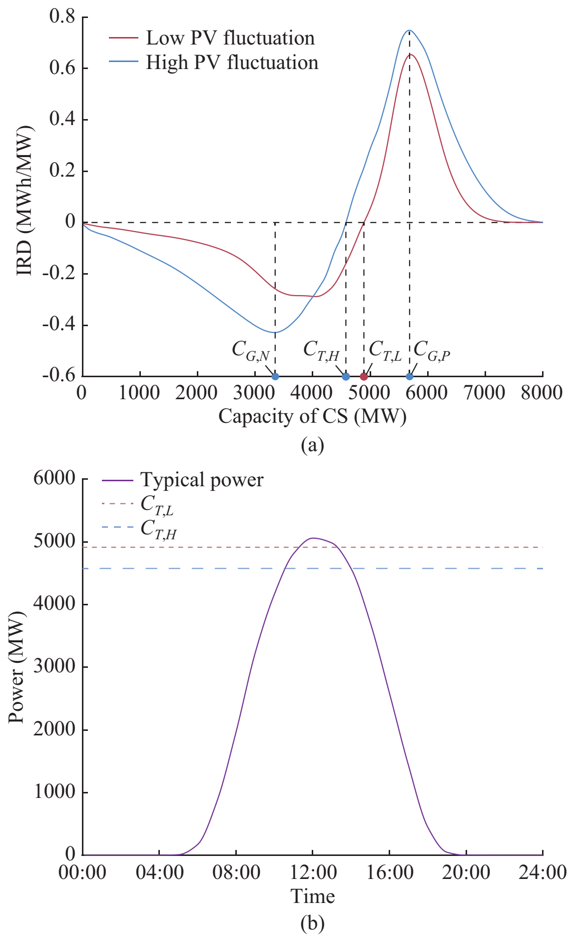

Fig. 11. Analysis for IRD curves. (a) IRD curves with different PV fluctuation amplitudes. (b) Relationship between transition capacity and typical PV generation.

In Fig. 11(a), the IRD curves show an evident trend. With the increase of capacity, the IRD decreases from zero to negative, then increases to positive, and finally decreases to zero. This variation process corresponds to the relative position of two CE-C curves in Fig. 10. When the capacity is sufficiently large or close to zero, the deterministic and stochastic CE-C curves tend to converge. However, in the middle range, the stochastic curve falls below the deterministic curve because the capacity restricts the PDF of $P_{C,t_h,t_d}^{\mathrm{CS,out}}$. To achieve the aforementioned variation, the IRD starts as negative, causing the stochastic CE-C curve to gradually fall below the deterministic CE-C curve. Subsequently, as the stochastic CE-C curve starts to align with the deterministic CE-C curve, the IRD shifts from negative to positive. After the two curves coincide, the IRD returns to zero.

The trend of the IRD curve can also be explained in terms of the CE revenue with increasing capacities. The IR, which denotes the increase in CE per unit of increased capacity, also indicates the revenue gained from the expanding capacity of CS. When the capacity is small (i.e., the output AC power is mostly constrained by the capacity of CS), increasing capacity of CS results in a smaller expected CE increment. This occurs as the capacity limits the probability of the input AC power, causing the negative impact of the uncertainties (reducing PV output) to be reflected in CE, while its positive impact (increasing PV output) is hindered by the capacity. In other words, enlarging the capacity of CS result in a smaller CE increase using the proposed method relative to the deterministic method, giving rise to the negative segment of the IRD curve. Conversely, when the capacity is large (i.e., the output power is mostly below the capacity of CS), the positive impact of the uncertainties is less likely to be limited by the capacity threshold. Therefore, the proposed method incorporates potential positive benefits, producing a larger expected CE increment, thereby accounting for the positive segment of the IRD curve.

Here, the capacity corresponding to the zero-crossing point of the IRD curve in Fig. 11(a) is defined as the transition capacity (denoted as C_T). Plot C_T in high PV fluctuation scenario (denoted as $C_{T,H}$) and low PV fluctuation scenario (denoted as $C_{T,L}$) with the typical PV output curve in the same graph, as shown in Fig. 11(b). According to Fig. 11(b), $C_{T,H}$ and $C_{T,L}$ are less than the peak value of the typical PV generation curve, and $C_{T,H}$ is less than $C_{T,L}$. These results can be explained as follows. As observed in Fig. 10, the IRD reaches its maximum value when IR of the deterministic CE-C curve approaches zero. For both high and low PV fluctuation scenarios, the deterministic CE-C curve remains the same. Therefore, the maximum values of the IRD curves for high and low PV fluctuation occur at nearly the same capacity ($C_{G,P}$ in Fig. 11(a)). Meanwhile, the magnitude of the PV fluctuation determines the peak value of IRD. The higher the PV fluctuation, the greater the peak value. Correspondingly, the higher fluctuation leads to a larger gap between C_T and $C_{G,P}$. Hence, $C_{T,H}$ is lower than $C_{T,L}$.

The IRD reflects the difference between the optimal capacity planning scheme calculated by proposed method (denoted by stochastic capacity, C_{sto}) and the optimal capacity planning scheme calculated by deterministic method (denoted by deterministic capacity, C_{dtm}). Assume that in a sending-end MT-HVDC system, the PV fluctuation varies in different regions where CSs are located. The CS with the highest PV fluctuation is analyzed and the graph of IRD can be plotted using analytical formulas. According to the EIR principle, the negative value of IRD indicates the lower planning capacity in the stochastic scenario, whereas the positive value indicates the opposite. Taking Fig. 11(a) as an example, the capacity corresponding to the maximum and minimum values of the IRD curve is defined as positive guideline capacity $C_{G,P}$ and negative guideline capacity $C_{G,N}$. The larger the absolute value of IRD, the greater the difference between the C_{sto} and C_{dtm}. When C_{dtm} is approximate to $C_{G,P}$ or $C_{G,N}$, the optimal capacity planning scheme calculated by the proposed method has a significant difference with that by deterministic method. When C_{dtm} is approximate to C_T, the difference is relatively small. To some extent, this difference indicates the superiority of the proposed method over the deterministic method. The closer the value of C_{dtm} is to the guideline capacities, the greater the benefits offered by the proposed method.

Additionally, the IRD curve can also be utilized to infer the optimal total capacity (i.e., C_{total}) of the sending-end MT-

HVDC system. In detail, the guideline capacities can be identified from the IRD curve. Subsequently, the IRs in the CE-C curve corresponding to the guideline capacities can be computed and used to determine the capacities of other CSs. Finally, summing the capacities of all CSs yields the optimal C_{total} of the sending-end MT-HVDC system. Although the optimization of the total capacity of sending-end MT-HVDC system offers a promising direction for future investigation, it lies outside the scope of this study.

The guideline for capacity planning can be summarized as follows. First, the stochastic CE-C curves and the IRD curve can be plotted using analytical formulas. According to the IRD curve, C_T, $C_{G,P}$, and $C_{G,N}$ are confirmed. Then, the optimal capacity planning scheme considering uncertainties can be obtained through the EIR principle performed on the stochastic CE-C curves. For the CS with the highest PV fluctuation, its optimal planning capacity tends to decrease in the stochastic scenario when C_{dtm} is lower than C_T, whereas it tends to increase when C_{dtm} is higher than C_T.

V. Case Studies

Case studies are conducted to verify the validity of the proposed method for CSs. The proposed method is implemented in MATLAB R2022b, and executed on an Intel(R) Core(TM) i9-10850K CPU 3.6 GHz with 64 GB RAM.

A. Calculation Parameters and Process

Calculations are performed on the four-terminal sending-end MT-HVDC system shown in Fig. 1. The typical PV output curves for different CSs are shown in Supplementary Material D Fig. SD1. The specific calculation process is demonstrated as follows, with corresponding flow chart shown in Fig. 12.

Step 1: obtain the typical PV output data ($365\times24\times1$).

Step 2: calculate the optimal capacity planning scheme using deterministic method. The result is saved as the deterministic planning scheme.

Step 3: calculate the optimal capacity planning using the proposed method. The result is saved as the stochastic planning scheme.

Step 4: generate 10000 sets of probabilistic PV output data. The spatial correlation is considered, with values shown in Supplementary Material D Table SDI. The longer the distance, the smaller the Pearson correlation coefficient value [29]. The temporal correlation coefficients are shown in Supplementary Material D Fig. SD2. These spatial and temporal correlation coefficients are computed according to the historical data.

Step 5: select one set of generated PV output data and calculate the CEs according to the deterministic planning scheme and stochastic planning scheme, respectively.

Step 6: check CE results and calculate the gap between the two CEs.

Step 7: once the last set of data is calculated (number of sets NS=10000), proceed to *Step 8*. If not, go to *Step* 5 and select a new set of data.

Step 8: analyze the results and plot the histogram of the CE difference between two methods.

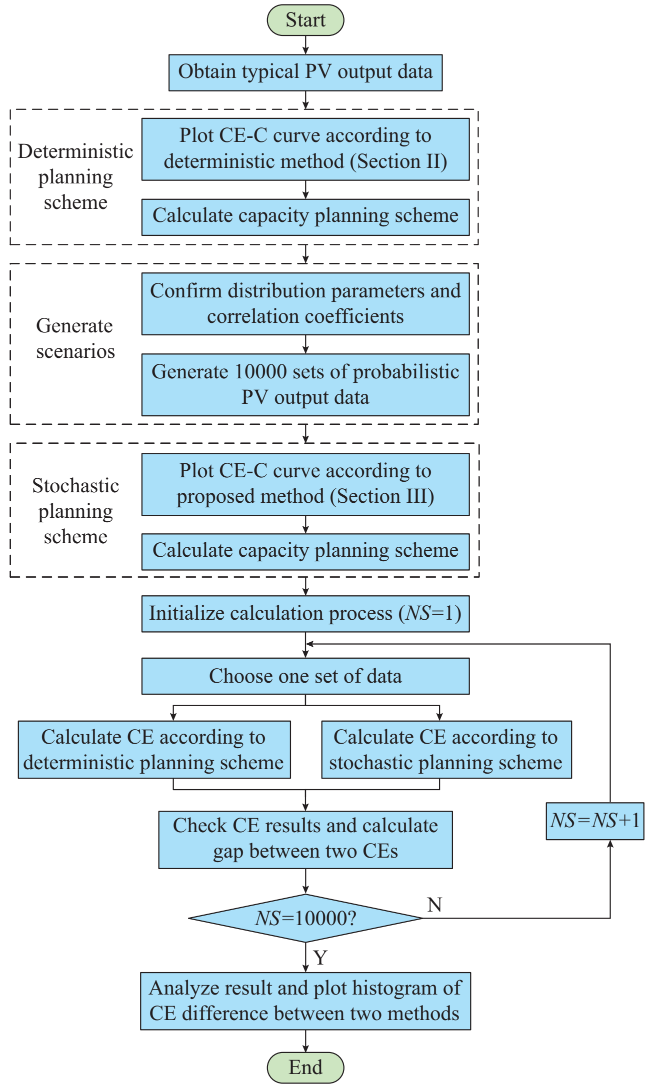

Fig. 12. Flow chart of calculation process.

Three cases are devised to demonstrate the superiority of the proposed method. C_{total} varies in three cases, namely 9500, 15000, and 20000 MW for cases 1, 2, and 3, respectively. For each case, calculations are performed following the flow chart in Fig. 12, and the results are presented in Table I and Fig. 13.

B. Results and Discussions

Table I shows the optimal capacity planning schemes of the three cases. Figure 13 depicts the CE difference between two methods, where C_{dtm} corresponds to the capacity (using deterministic method) of CS 2 in Table I. The x-axis of Fig. 13(b) indicates the CE calculated by the proposed method minus the CE of the deterministic method. The positive value indicates that the proposed method can convert more energy than the deterministic method. The results in histograms can be formulated by a normal distribution because of the normal-distributed stochastic CEs (Section III-B).

For case 1, the planning capacity of CS 2 using the proposed method is smaller than that of deterministic method, whereas the result is reversed in case 3.

TABLE I
OPTIMAL CAPACITY PLANNING SCHEME OF CASE STUDIES

Case No.	Calculation method	Capacity planning scheme (MW)				Expectation of CE (TWh)
		CS 1	CS 2	CS 3	CS 4	
1	EIR performed on deterministic CE-C	2123	3326	1298	2753	28.528
	EIR performed on stochastic CE-C	2235	3112	1350	2803	28.546
2	EIR performed on deterministic CE-C	3731	4506	2213	4550	37.679
	EIR performed on stochastic CE-C	3714	4561	2209	4516	37.681
3	EIR performed on deterministic CE-C	5011	5737	3014	6238	40.970
	EIR performed on stochastic CE-C	4882	6151	2921	6046	41.016

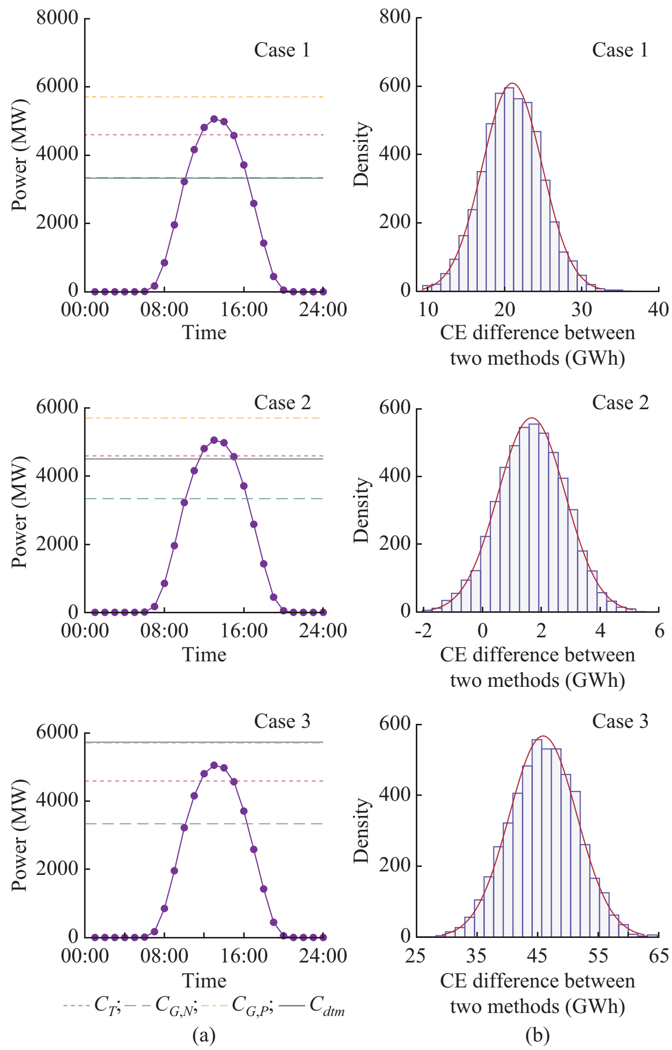

Fig. 13. Results of three cases. (a) Values of transition capacity, deterministic capacity, and guideline capacities. (b) Histograms of CE differences.

In addition, by comparing the histograms of case 1 and case 3 with that of case 2, the CE difference in case 2 has more negative values. The reason is that C_{dtm} in case 1 and case 3 is approximate to the guideline capacities $C_{G,N}$ or $C_{G,P}$, and in case 2, it is approximate to C_T. Nevertheless, the expectations of these results are all greater than zero. Such results correspond to the analysis for IRD curves in Section IV. Moreover, these results indicate that the proposed method performs better than the deterministic method, and the stochastic schemes can collect the most expected CE.

C. Practical Application Analysis

Due to unpredictable uncertainties in different scenarios, it is challenging to model probabilistic PV generation accurately with predefined distributions [30]. This means the actual PV output tends to be more irregular and complex. Therefore, some noises are introduced into the Beta-distributed PV output data, as shown in Fig. 14(a). The detailed generation process of PV output data is shown as follows.

Step 1: generate a set of Beta-distributed PV output data.

Step 2: process the historical data to obtain the dataset of the PV fluctuation (actual values minus the mean).

Step 3: extract random samples from the fluctuation dataset to produce the noise data.

Step 4: the noise data and the generated Beta-distributed PV output data are added together to create a new set of data representing the actual scenarios.

The R^2 value indicates the fitness of the generated data to a Beta distribution. Use these data to replace the calculated data in case 1 and do the same calculation process. The results are shown in Fig. 14(b) and (c).

In Fig. 14(b), the CE difference calculated by the 75.5% R^2 datasets (blue color results) is smaller than that of 99.2% R^2 datasets (yellow color results). This means the noise in generated data has a negative impact on the CE profits, and this negative impact is represented by the ratio of the expected CE of the data with noise to that of no-noise data. As shown in Fig. 14(c), the lower the ratio, the greater the negative impact. Despite this, the expectation is still greater than zero, and this indicates that the proposed method is still superior to the deterministic method.

In practical projects, the rated capacities of CSs are usually regulated to some typical discrete values, such as an integral multiple of 500 MW. It indicates the theoretical optimal capacities calculated by the proposed method need to be revised to these typical values and this process may cause some differences in the planning schemes. Considering the large capacities of the CSs for practical projects, the differences can be ignored in most cases. As a consequence, the method of selecting these typical values for practical projects is not discussed in this paper and could be studied in future works.

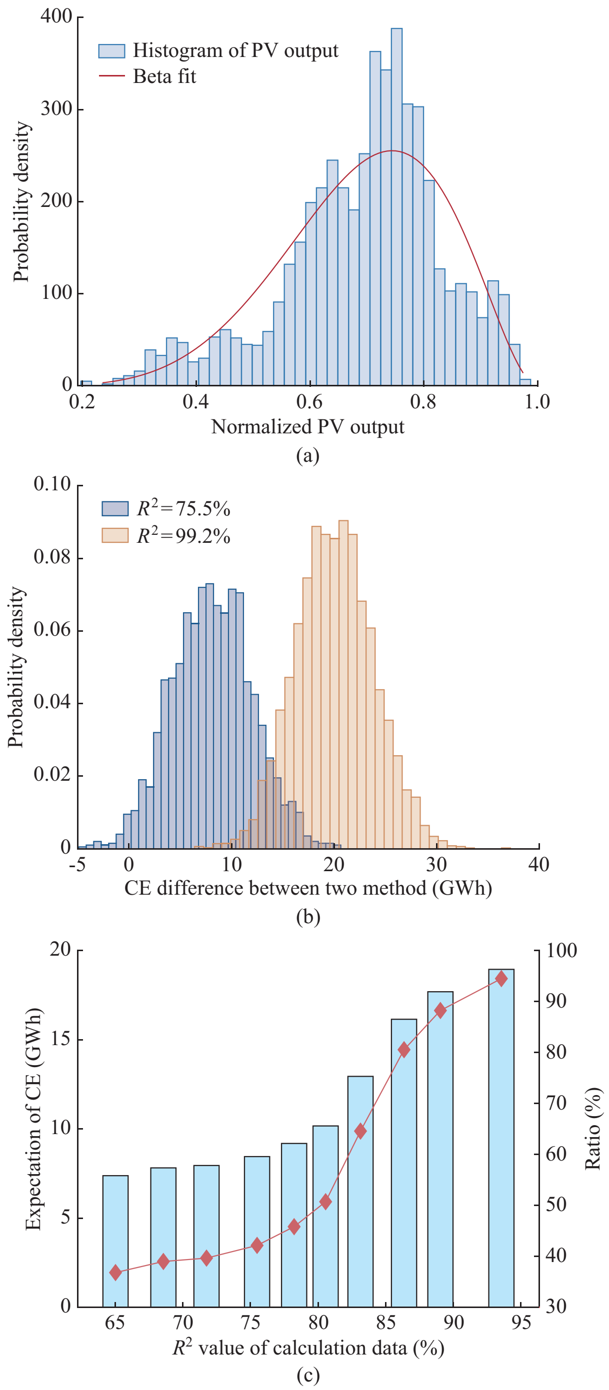

Fig. 14. Calculation results of PV output data with noises. (a) Beta-distributed data with noises. (b) Calculation result of datasets with different R^2 values. (c) Expectation of CE and its ratio to result of no-noise scenario.

VI. Conclusion

This paper presents an optimal capacity planning method for CSs, incorporating the uncertainties of PV generation. Analytical formulas are derived to describe the probabilistic results of CEs, and their correctness is verified through computational experiments. The optimal capacity planning scheme can be obtained through EIR principle, which is performed on the stochastic CE-C curves.

A general guideline for capacity planning is proposed, in which the optimal capacity of CS in stochastic scenarios tends to decrease when its C_{dtm} is smaller than C_T, whereas it increases when C_{dtm} is larger than C_T. This guideline validates the capacity planning results and also indicates the value brought by PV fluctuations. Finally, several case studies demonstrate the superiority of the proposed capacity planning method.

In future works, the investment and construction costs of the CSs could be incorporated to develop a more comprehensive method for optimal capacity planning.

References

[1] J. Feng, W. Xiang, J. Wen *et al.*,“Mid- and high-frequency resonance characteristics and suppression strategies of VSC-UHVDC for large-scale renewable energy transmission,” *Journal of Modern Power Systems and Clean Energy*, vol. 12, no. 6, pp. 2058-2070, Nov. 2024.

[2] Q. Wang, L. Yao, J. Xu *et al.*, “Steady-state voltage security-constrained optimal frequency control for weak HVDC sending-end AC power systems,” *Journal of Modern Power Systems and Clean Energy*, vol. 12, no. 2, pp. 658-669, Mar. 2024.

[3] H. Pang and X. Wei, “Research on key technology and equipment for Zhangbei 500 kV DC grid,” in *Proceedings of 2018 International Power Electronics Conference*, Niigata, Japan, May 2018, pp. 2343-2351.

[4] J. Li, B. Zhu, Y. Guo *et al.*, “The simulation of kunliulong flexible DC project with single station operation and out of operation,” in *Proceedings of 2021 IEEE/IAS Industrial and Commercial Power System Asia*, Chengdu, China, Jul. 2021, pp. 1028-1034.

[5] F. Palombi, L. Piegari, S. Drco *et al.*, “Impact on power system frequency dynamics from an HVDC transmission system with converter stations controlled as virtual synchronous machines,” in *Proceedings of 2019 IEEE Milan Power Tech*, Milan, Italy, Jun. 2019, pp. 1-6.

[6] E. Pierri, O. Binder, N. Hemdan *et al.*, “Challenges and opportunities for a European HVDC grid,” *Renewable and Sustainable Energy Reviews*, vol. 70, pp. 427-456, Apr. 2017.

[7] X. Zhang, M. Ou, Y. Song *et al.*, “Review of Middle East energy interconnection development,” *Journal of Modern Power Systems and Clean Energy*, vol. 5, no. 6, pp. 917-935, Nov. 2017.

[8] H. Xie, Z. Bie, and G. Li, “Reliability-oriented networking planning for meshed VSC-HVDC grids,” *IEEE Transactions on Power Systems*, vol. 34, no. 2, pp. 1342-1351, Mar. 2019.

[9] S. Torbaghan, M. Gibescu, B. Rawn *et al.*, “Investigating the impact of unanticipated market and construction delays on the development of a meshed HVDC grid using dynamic transmission planning,” *IET Generation, Transmission & Distribution*, vol. 9, no. 15, pp. 2224-2233, Nov. 2015.

[10] C. Bittar, A. Pacarar, K. Sorto-Ventura *et al.*, “A study of the potential for a submarine interconnection in the gulf of St. Lawrence,” in *Proceedings of 2019 IEEE Electrical Power and Energy Conference*, Montreal, Canada, Oct. 2019, pp. 1-6.

[11] Y. Liu, J. Cui, L. Li *et al.*, “Study on the optimal capacity allocation of converter stations for flexible DC interconnection systems in multi-distribution areas,” in *Proceedings of 18th International Conference on AC and DC Power Transmission*, Online Conference, Jul. 2022, pp. 1-5.

[12] K. Xie, J. Dong, H. Tai *et al.*, “Optimal planning of HVDC-based bundled wind-thermal generation and transmission system,”*Energy Conversion and Management*, vol. 115, pp. 71-79, May 2016.

[13] S. Karaki, R. Chedid, and R. Ramadan, “Probabilistic performance assessment of autonomous solar-wind energy conversion systems,” *IEEE Transactions on Energy Conversion*, vol. 14, no. 3, pp. 766-772, Sept. 1999.

[14] A. Zakaria, F. Ismail, M. Lipu *et al.*, “Uncertainty models for stochastic optimization in renewable energy applications,”*Renewable Energy*, vol. 145, p. 154571, Jan. 2020.

[15] H. Zhang, J. Shen, and G. Wang, “Day-ahead stochastic optimal dispatch of LCC-HVDC interconnected power system considering flexibility improvement measures of sending system,” *International Journal of Electrical Power & Energy Systems*, vol. 138, p. 107937, Jun. 2022.

[16] B. Li and J. Li, “Probabilistic sizing of a low-carbon emission power system considering HVDC transmission and microgrid clusters,” *Applied Energy*, vol. 304, p. 117760, Dec. 2021.

[17] Y. Wen, Y. Lu, J. Gou *et al.*, “Robust transmission expansion planning

of ultrahigh-voltage AC-DC hybrid grids," *IEEE Transactions on Industry Applications*, vol. 58, no. 3, pp. 3294-3302, May 2022.

[18] S. Jiang, S. Gao, G. Pan *et al*., "A novel robust security constrained unit commitment model considering HVDC regulation," *Applied Energy*, vol. 278, p. 115652, Nov. 2020.

[19] H. Lin, L. Liang, and H. Yi, "Study on the optimal capacity planning method of converter stations for sending-end multi-terminal HVDC transmission grid," in *Proceeding of 2023 IEEE PES Innovative Smart Grid Technologies-Asia*, Auckland, New Zealand, Nov. 2023, pp. 1-5.

[20] B. Wang, W. Cao, J. Gao *et al*., "Optimized load distributed of power plant units based on the improved equal incremental principle," in *Proceedings of 2005 International Conference on Machine Learning and Cybernetics*, Guangzhou, China, Aug. 2005, pp. 1094-1098.

[21] Chinese Government. (2024, Aug.). National meteorological information center. [Online]. Available: https://data.cma.cn/data/

[22] D. Kumar and B. Padhy, "Optimal selection of voltage controlling parameter in uncertain active distribution network," *IEEE Transactions on Industry Applications*, vol. 60, no. 1, pp. 1576-1588, Jan. 2024.

[23] D. Khatod, V. Pant, and J. Sharma, "Evolutionary programming based optimal placement of renewable distributed generators," *IEEE Transactions on Power Systems*, vol. 28, no. 2, pp. 683-695, May 2013.

[24] U. Ramadhani, M. Shepero, J. Munkhammar *et al*., "Review of probabilistic load flow approaches for power distribution systems with photovoltaic generation and electric vehicle charging," *International Journal of Electrical Power & Energy Systems*, vol. 120, p. 106003, Sept. 2020.

[25] Z. Ren, W. Yan, X. Zhao *et al*., "Chronological probability model of photovoltaic generation," *IEEE Transactions on Power Systems*, vol. 29, no. 3, pp. 1077-1088, May 2014.

[26] M. Fan, V. Vittal, G. Heydt *et al*., "Probabilistic power flow studies for transmission systems with photovoltaic generation using cumulants," *IEEE Transactions on Power Systems*, vol. 27, no. 4, pp. 2251-2261, Nov. 2012.

[27] F. Fan, X. Zhou, L. Zhang *et al*., "Modeling multi-temporal correlation of PV stations output *via* improved nonparametric disaggregation method in power system reliability evaluation," *IEEE Access*, vol. 12, pp. 109071-109079, Aug. 2024.

[28] A. De, "Beyond the central limit theorem: asymptotic expansions and pseudorandomness for combinatorial sums," in *Proceedings of 2015 IEEE 56th Annual Symposium on Foundations of Computer Science*, Berkeley, USA, Oct. 2015, pp. 883-902.

[29] H. Wu, Y. Yuan, J. Zhu *et al*., "Potential assessment of spatial correlation to improve maximum distributed PV hosting capacity of distribution networks," *Journal of Modern Power Systems and Clean Energy*, vol. 9, no. 4, pp. 800-810, Jul. 2021.

[30] Y. Shi and N. Chen, "Conditional kernel density estimation considering autocorrelation for renewable energy probabilistic modeling,"*IEEE Transactions on Power Systems*, vol. 36, no. 4, pp. 2957-2965, Jul. 2021.

Hao Lin received the B.E. degree in electrical engineering from Harbin Institute of Technology, Shenzhen, China, in 2023. He is currently pursuing the Ph.D. degree in Harbin Institute of Technology. His research interests include optimal operation and planning for power system with high penetration rate of renewable energy.

Liang Liang received the B.E. degree in electrical engineering from Tsinghua University, Beijing, China, in 2005, the M.S. degree in electrical engineering from the Institute of Electrical Engineering, Chinese Academy of Sciences, Beijing, China, in 2008, and the Ph.D. degree in electrical engineering from the University of Hong Kong, Hong Kong, China, in 2016. He is an Senior Member of IEEE. He is currently an Associated Professor in Harbin Institute of Technology, Shenzhen, China. His research interests include power system resilience, power system flexibility, and renewable energy integration.

Haiqiong Yi received the Ph.D. degree in electrical engineering from Huazhong University of Science and Technology, Wuhan, China. She is currently a Senior Engineer with the State Grid Economic and Technological Research Institute Co., Ltd., Beijing, China. Her research interests include power system planning method and electricity market.

Xiangjun Kong received the M.S. degree in automation engineering from Shanghai Jiao Tong University, Shanghai, China. She is currently working as a Senior Economist at State Grid Shanghai Municipal Electric Power Company, Shanghai, China. Her research interests include power system planning with renewable energy integration.